

# Bulk micro-defect detection with low-angle illumination

Cite as: Rev. Sci. Instrum. 92, 043701 (2021); doi: 10.1063/5.0027147

Submitted: 3 September 2020 • Accepted: 14 March 2021 •

Published Online: 2 April 2021



View Online



Export Citation



CrossMark

T. Szarvas,<sup>1,a)</sup> G. Molnár,<sup>1</sup> Gy. Nádudvari,<sup>1</sup> Sz. Tóth,<sup>1</sup> O. Almásy,<sup>1</sup> Sz. Spindler,<sup>1</sup> D. Erdei,<sup>1</sup> Sz. Pothorszky,<sup>1</sup> R. Kretschmer,<sup>2,b)</sup> and S. Bauer<sup>2</sup>

## AFFILIATIONS

<sup>1</sup>Semilab Co. Ltd., Prielle Kornélia u. 4/A, 1117 Budapest, Hungary

<sup>2</sup>Siltronic AG, Einsteinstraße 172, 81677 Munich, Germany

<sup>a</sup>Author to whom correspondence should be addressed: [tamas.szarvas@semilab.hu](mailto:tamas.szarvas@semilab.hu)

<sup>b</sup>Electronic mail: [Robert.Kretschmer@siltronic.com](mailto:Robert.Kretschmer@siltronic.com)

## ABSTRACT

The detection of oxygen precipitates, voids, and other defects is critical for semiconductor wafer makers. One of the industry standard techniques for detecting these Bulk Micro-Defects (BMDs) is Semilab's Light Scattering Tomograph (LST) system. In this measurement, unpatterned wafers are nominally cleaved in half. Illumination is applied to the front surface of the sample, and the light scattered off of the defects is collected via the cleaved surface. This technique had been limited to the measurement of unpatterned wafers, but device makers show significant interest in measuring BMD distributions on patterned wafers using scattering-based techniques. A pattern on the surface of the wafer can cause significant scattering, making the standard LST technique unsuitable for this task. We present a solution for patterned wafer BMD measurements by an addition of a low-angle illumination unit to the standard LST system. This new illumination unit focuses the light into the bulk of the wafer via the cleaved surface, which enables measurement on patterned samples. The new system is called "light scattering tomograph enhanced by low-angle illumination." Excellent correlation was found between the detected defect densities obtained by the low-angle and the standard LST illumination mode.

Published under license by AIP Publishing. <https://doi.org/10.1063/5.0027147>

## I. INTRODUCTION

Light Scattering Tomography (LST) is used for the detection of oxygen precipitations,<sup>1,2</sup> voids,<sup>3</sup> and any objects, which produce a scattered light signal<sup>4,5</sup> in silicon wafers. Defects that can be detected with LST are sometimes abbreviated to LSTDs<sup>6</sup> but are more commonly known as Bulk Micro-Defects (BMDs). In addition to BMDs, LST has also been applied to find dislocations.<sup>7</sup> This technique has a history in silicon wafer production.<sup>8,9</sup> Samples are cleaved in half for the measurement and illuminated from the front surface. The scattered light produced by BMDs in the bulk of a silicon (Si) wafer is collected via the cleaved surface by a camera. The arrangement of the setup is illustrated in Fig. 1(a). The number, the density ( $\text{cm}^{-3}$ ), the size of the defects, and the denuded zone<sup>10</sup> are determined via an automated image processing algorithm. A well-detailed summary and comparison to other methods are found in Ref. 10, while specific topics of the detection are reported in Refs. 11 and 12. Many silicon wafer manufacturers use such tools to characterize ingots and wafers for process control. The technique is also being used by

monocrystalline silicon photovoltaic cell manufacturers as they continue to improve the efficiency of their cells.<sup>13</sup>

Typically, device makers push the task of monitoring the BMDs onto the wafer makers who supply their substrates. However, device manufacturers have recognized the need to characterize the BMD distribution in their incoming wafers, as well as for failure analysis. The failure analysis application is challenging, as the wafers are typically patterned. The scattering from the pattern on the surface negatively impacts the LST measurement. If the back surface of a sample is polished, measurement can be attempted from this side by using the standard LST tool; however, the success of this method depends on the ability of light to penetrate the full wafer thickness. The back surface may be matte or may have some other properties, which make the LST measurement difficult or impossible. Reference 10 details some methods used to overcome these problems.

Semilab has also been running development programs to provide solution(s). A possible solution is the Envision-3000 system, which detects buried defects based on defect-band

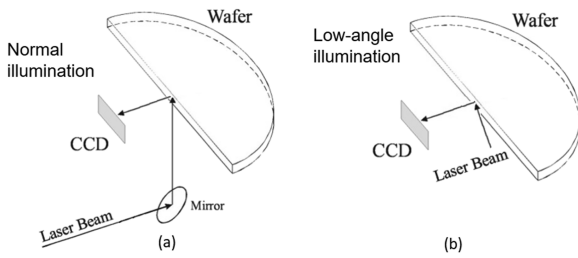


FIG. 1. Schematic representation of normal and low-angle illuminations.

photoluminescence emission.<sup>14</sup> The Envision technique can detect buried defects in processed wafers without cleaving, but it requires a test area without metallization to be able to optically illuminate the bulk of the sample.

In this paper, we present a new scattering-based tool for patterned wafer inspection. Both the illumination and detection are applied via the cleaved surface, keeping the dark field configuration (the two light paths are spatially separated). A microscope is held perpendicular to the cleaved surface while the illumination is applied at a low angle, as depicted in Fig. 1(b).

This metrology system is named “Light Scattering tomograph enhanced by Low-angle illumination (LSL).” This instrument contains both the normal illumination mode (identical to LST illumination) and low-angle illumination mode for measurement on both unpatterned and patterned wafers. The low-angle illumination mode has been validated against the normal illumination mode with a strong correlation.

Section II details the mechanical and optical design of the system. Measurement results and correlation data are shown in Secs. III and IV, respectively.

## II. SYSTEM DESIGN

### A. Design of a standard LST system

An LST system uses a dark field imaging system to detect BMDs. The sample is cleaved in half and illuminated from the front surface, and the scattered signal from defects is detected via the cleaved surface. The illumination is applied perpendicularly to the imaging system, as shown in Fig. 2.

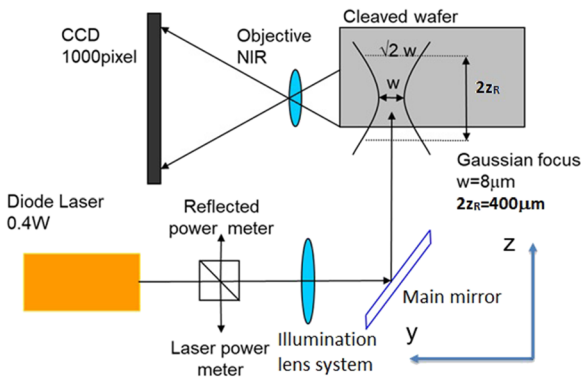


FIG. 2. Schematic layout of an LST system (side view).

A  $\lambda \approx 1 \mu\text{m}$  wavelength was chosen to optimize for deep penetration in silicon while keeping a strong scattered light signal ( $I \propto 1/\lambda^4$ ). The laser source is a fiber-coupled laser diode, and the mode field diameter inside the single-mode fiber is  $6.6 \pm 0.3 \mu\text{m}$ . For Gaussian beams, the formula for the angular radius ( $\theta$ ) is

$$\theta = \frac{\lambda}{\pi w_0} \approx 0.1, \quad (1)$$

where  $w_0$  is the beam waist, approximated as the half of the mode field diameter. A lens system and a mirror are used to focus the beam inside the sample. The illumination beam is focused in a cone shape such that the beam diameter at the focal point is  $2w_0 = 8.2 \approx 8 \mu\text{m}$ . The distance the collimated waist region of the light beam extends is twice the Rayleigh range,

$$2z_R = 2 \frac{\pi w_0^2}{\lambda} \approx 400 \mu\text{m}. \quad (2)$$

The illumination beam can be approximated as a cylinder with a constant thickness of  $8 \mu\text{m}$  situated  $\approx 100 \mu\text{m}$  depth of the bulk from the cleaved surface.

A high Numerical Aperture (NA = 0.65) objective is used to capture the light from the bulk. The Depth of Field (DoF) of the objective is

$$\text{DoF} = \frac{\lambda}{\text{NA}^2}. \quad (3)$$

In the air, it corresponds to  $\approx 2.5 \mu\text{m}$ , while inside the Si material, the DoF is elongated by the refractive index ( $n \approx 3.5$ ): DoF  $\approx 9 \mu\text{m}$ . This value is in good agreement with the beam diameter, i.e., all defects in the focal plane are illuminated. The maximum field of view of the objective lens is  $440 \mu\text{m}$ . The thickness of a wafer is usually  $\approx 700 \mu\text{m}$ , from which  $400 \mu\text{m}$  object height is magnified and projected into the camera to get a pixel resolution of  $0.44 \mu\text{m}$ , which is fine enough to resolve the Airy disk of the detected defects. As depicted in Fig. 2, the illumination beam is optimized in the system, as the double of its Rayleigh range is in agreement with the object height ( $400 \mu\text{m}$ ).

The measurement image is taken by using the CCD camera in a continuous line-scanning mode. The wafer is being moved in the  $x$ -direction synchronously with the camera readout speed, and the two-dimensional image is taken row-by-row. Due to the line-scanning mode, the illumination beam is integrated over the  $x$ -direction. The length of the image depends on the length of the movement.

### B. Design of the new LSL system

In an LSL system, a different collection objective is used with a longer working distance to accommodate for the low-angle illumination unit. The NA of this objective lens is 0.45, which indicates that the DoF  $\approx 18 \mu\text{m}$  [see Eq. (3)].

The LSL system contains two separate illumination units: the traditional perpendicular unit used in traditional LST systems and the low-angle illumination unit used for patterned wafer measurements. For the perpendicular mode, it is worth noting that only a portion of the DoF is illuminated (8 out of  $18 \mu\text{m}$ ). In the low-angle mode, the illumination line is generated via the cleaved surface by a cylindrical lens with a focal length of 8 mm (see Fig. 3).

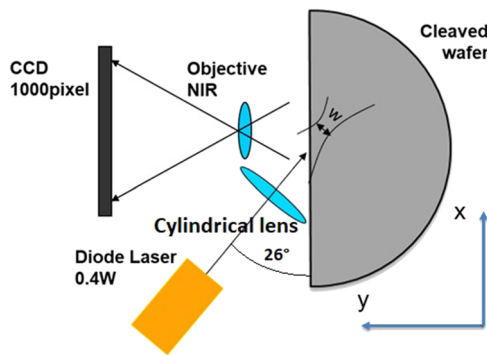


FIG. 3. Arrangement of the components for low-angle illumination (top view).

A  $500\text{ }\mu\text{m}$  high aperture was used in the  $z$ -direction in the low-angle illumination unit together with very precise height adjustment to position the beam inside the wafer without illuminating the cleaved edges. The optics of the illumination were designed to create a homogeneous intensity profile along the focused line in the  $z$ -direction. The illumination is applied at a low angle of  $26^\circ$  to the cleaved surface of the wafer (see Fig. 3). We keep  $\approx 10^\circ$  free for mechanical mounting and clearance. The microscope objective working distance constrains the space, which can be used for the line generation in low-angle illumination. The half angle of the focused beam of the low-angle illumination is  $16^\circ$ , and together with a  $10^\circ$  spacer, we obtain the selected value:  $26^\circ$ .

Due to the refraction occurring when the low-angle light beam enters the wafer, the direction of propagation in the bulk has an angle of about  $15^\circ$  to the optical axis of the microscope unit (perpendicular to the cleaved surface). This considerable difference in the direction of light propagation is caused by the high refractive index of Si ( $n \approx 3.5$ ). Figure 4 depicts the situation in detail.

A cylindrical lens focuses the low-angle illumination beam into a line. Defects are illuminated throughout the beam path, both inside and outside of the focal plane. These regions can be seen in Fig. 4: the parts of the beam top left and bottom right to the object plane. As different depth positions are illuminated, defects in out-of-focus positions appear to be defocused in the image sensor. These defocused defects can mask the well-focused defects. A narrow slit is applied in an intermediate image plane in the microscope unit to filter these defocused defects out. This slit filters the light in the lateral direction. Since the illumination is tilted, it filters the light in the depth direction as well (see Fig. 4). With this slit, the majority of the imaged illuminated area is concentrated in the  $\pm 10\text{ }\mu\text{m}$  region in depth around the object plane. Only a small portion of the illumination extends up to a  $\pm 15\text{--}20\text{ }\mu\text{m}$  thick volume.

Figure 4 shows the situation where the illumination is concentrated at  $\approx 100\text{ }\mu\text{m}$  in depth. The illuminated part of the cleaved surface is excluded by the aperture mentioned above. The instrument was optimized for a  $100\text{ }\mu\text{m}$  depth, but it is possible to adjust for other depths. Deeper positions are limited by increased spherical aberration and light loss from optical absorption. Shallower positions will not exclude the cleaved surface, and inevitably, there will be particles on the cleaved surface, which will show up as defocused

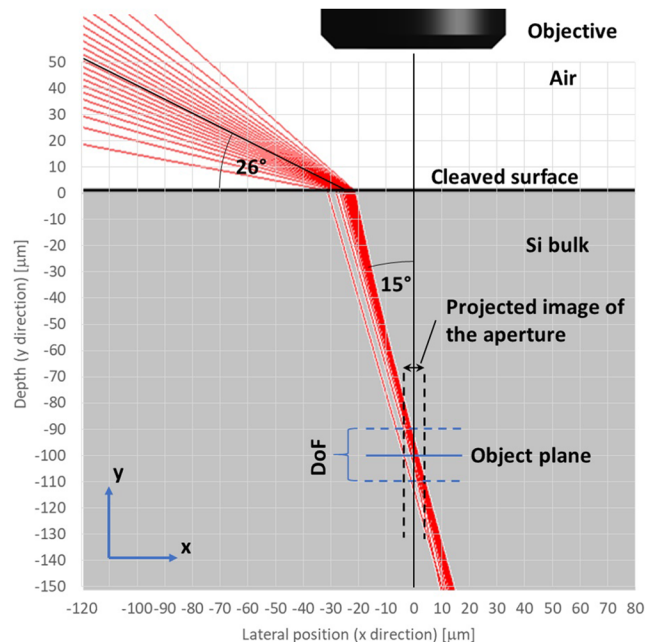


FIG. 4. Low-angle illumination (top view). The size and distance of the objective are not scaled. The image of the objective should be considered only as an illustration of the detection.

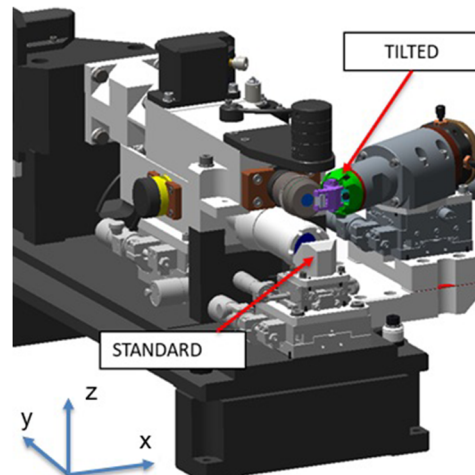


FIG. 5. Design of the final optical unit.

defects in the measured image. This effect can mask defects in the bulk, leading to inaccurate measurements.

The design of the final optical unit is shown in Fig. 5.

### III. MEASUREMENT RESULTS

Both the perpendicular and low-angle modes are adjusted to position the beam waist at the same depth ( $y$ ) from the cleaved surface and in the same horizontal ( $x$ ) position. The optical microscope is adjusted to focus on this area.

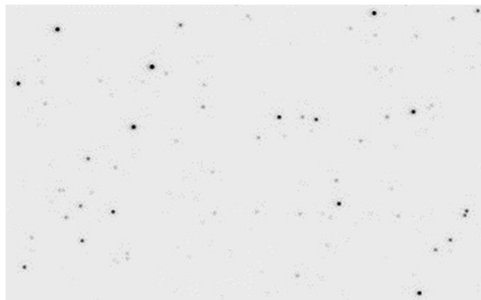


FIG. 6. Example measurement image with normal illumination.

Normal and low-angle results from the same position on a medium density wafer ( $1 \times 10^8$ – $1 \times 10^{10}$  cm $^{-3}$ ) are presented in Figs. 6 and 7. In each case, the image size is  $162 \times 100$   $\mu\text{m}^2$  with a pixel resolution of  $0.44 \mu\text{m}$ . Defects included in the normal image (Fig. 6) can also be found in the same position in the low-angle image (Fig. 7), but the low-angle image shows defects not contained in the normal image. Figure 8 shows a combined image with the defects found in the normal mode (blue), the defects found in the low-angle mode (red), and the defects seen in both (black).

Figure 8 shows that the illumination of the normal mode and the low-angle mode is set at the same depth from the cleaved surface. Few defects were found, which appear only in the normal mode image (blue defects). Almost all defects detected in the normal mode are also visible in the low-angle image (black defects). The number of defects detected only in the low-angle mode (red defects) is 2–3 times higher than the number of defects detected in both modes (black defects). This difference in defect count indicates that a 3–4 times larger volume is illuminated in the low-angle mode than in the normal mode. A thickness calibration factor can be used for density calculations to compensate for this difference. A correlation study detailed in Sec. IV was carried out to determine what this factor should be.

In a low-angle image, defects in the background are also illuminated slightly, since the thickness of the illuminated volume is in the range of  $\pm 15$ – $20 \mu\text{m}$ , as shown in Sec. II B. As the DoF of the objective is only  $\pm 9 \mu\text{m}$ , these low-intensity defects appear to be defocused in the image. These defocused defects can be filtered out by using an

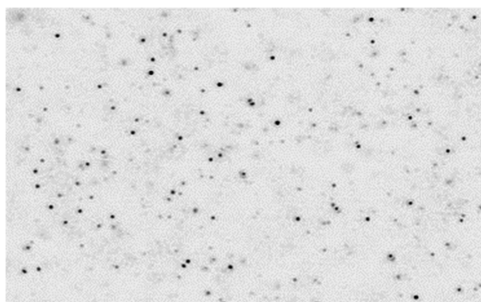


FIG. 7. Example measurement image with low-angle illumination.

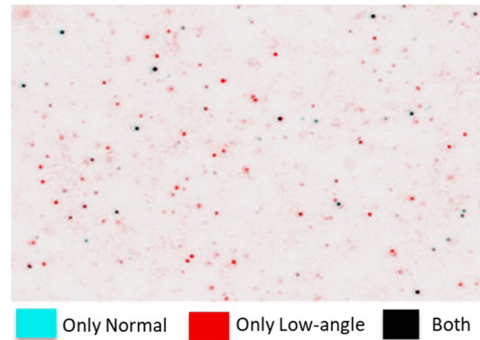


FIG. 8. Merged image where defects are colored based on their occurrence.

appropriate image processing algorithm. An automatic defect recognition algorithm based on filtering for the signal-to-noise ratio of the defects was applied to these images. Figure 9 depicts the operation of the automatic defect finding algorithm in the low-angle image. Defects with a strong signal in the focal plane are found, and less focused defects in the background are filtered out.

#### IV. CORRELATION WITH LST

The density of the defects in an image is calculated by using the following formula:

$$\mathcal{D} = \frac{\#}{AT}, \quad (4)$$

where symbol  $\#$  is a notation for the number of defects found by the automatic defect finding algorithm,  $A$  is the area of the image, and  $T$  is the thickness. The thickness for the normal mode is defined by  $T_{\text{norm}} = f_{\text{th}} 2w$ , where  $2w$  is the beam diameter at the focal point and  $f_{\text{th}}$  is the thickness factor, which is determined by correlation measurements. For the low-angle illumination, the thickness is denoted by  $T_{\text{low}}$ , which is also determined by correlation measurements.

To validate the reported density in low-angle illumination, we compare it to normal illumination density data after calibration by a thickness factor. This calibration was carried out by applying a linear regression on data acquired on a sample set provided by Siltronic AG. The sample set was designed to cover a large density range while remaining relevant to real-world products. The wafers in the sample set were measured at different radial positions. Figure 10 presents

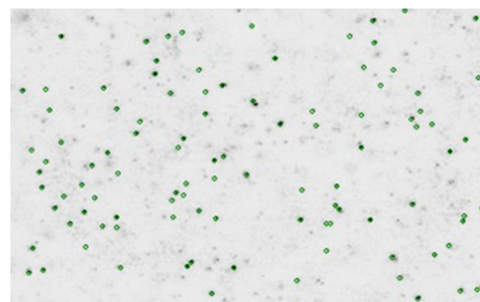


FIG. 9. Automatically detected defects in the low-angle illumination image.

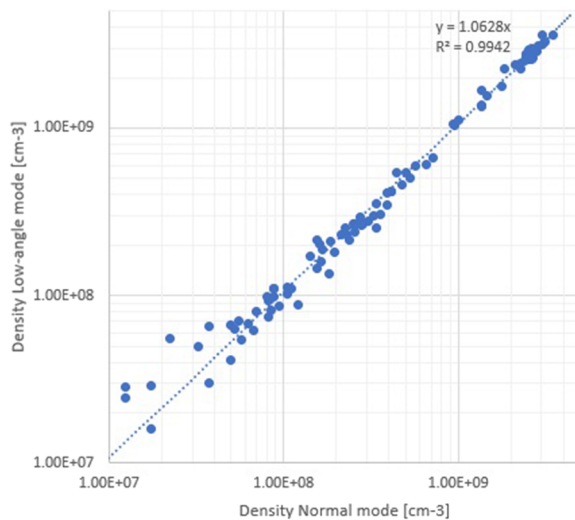


FIG. 10. Correlation between normal and low-angle illumination modes after density calibration.

the excellent correlation between normal and low-angle illumination modes after successful density calibration.

The covered density range is  $1 \times 10^7$ – $5 \times 10^9$  cm<sup>-3</sup>. The axes are in logarithmic scale for better visualization. The slope is 1.06, and  $R^2$  is 0.99. The thickness factor for low-angle illumination was calculated to be four times larger than that for the normal mode:  $T_{\text{low}} = 4T_{\text{norm}}$ . This dataset shows that the density correlation is strong between the two modes.

To align the density with standard LST tools, an absolute calibration is still necessary. We used the LST golden reference tool at Semilab and another density correlation set to do this. These wafers form a density ladder with closely equidistant steps. After the successful absolute calibration, we performed measurements with the

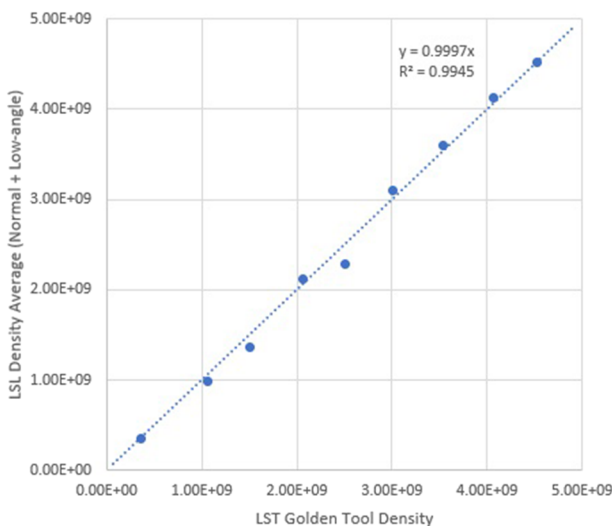


FIG. 11. Absolute calibration of the LSL tool to the LST golden tool.

LSL tool in both normal and low-angle modes and compared the average density of the two modes to the LST golden tool results. The results can be seen in Fig. 11, showing excellent absolute correlation with a near 1:1 relationship.

## V. CONCLUSION

This work demonstrates the capability of the LSL tool—a scattering-based imaging system for characterizing BMDs in silicon wafers. The low-angle illumination feature enables measurement on both unpatterned and patterned wafers. The equipment contains a normal incidence mode, equivalent to a traditional LST measurement, and a low-angle mode, which allows for the patterned wafer measurement. The two modes were shown to provide equivalent results after a calibration factor was derived and applied.

In Sec. II, the engineering concept is shown in detail for both the normal and low-angle modes. In the normal mode, only a part of the depth of field is illuminated (8 from 18 μm), while in the low-angle mode, the full DoF is illuminated. Figure 5 shows the final system design containing the normal and low-angle illumination units.

In Sec. III, measurement images are compared in both the low-angle and normal mode operation. Images were taken in the same measurement position to validate the optical alignment. The beams generated by the two illumination units are focused in the same depth from the cleaved wafer surface. The defects visible in the normal image are also visible in the low-angle image, as shown in Fig. 8.

In Sec. IV, the correlation between the two illumination modes is presented by determining the correct measured thickness for each case. Excellent correlation is demonstrated across a commercially relevant density range. The LSL tool results were also compared to Semilab's LST golden tool, which is used to calibrate the fleet of worldwide instruments. A strong correlation was shown in this case as well. The LSL tool can be used for BMD detection on both normal and patterned wafers and provides equivalent results to the widely accepted LST tools.

## DATA AVAILABILITY

The data that support the findings of this study are available from the corresponding author upon reasonable request.

## REFERENCES

- <sup>1</sup>S. Umeno, Y. Yanase, M. Hourai, M. Sano, Y. Shida, and H. Tsuya, "Dependence of grown-in defect behavior on oxygen concentration in Czochralski silicon crystals," *Jpn. J. Appl. Phys., Part 1* **38**, 5725 (1999).
- <sup>2</sup>S. Umeno, S. Sadamitsu, H. Murakami, M. Hourai, S. Sumita, and T. Shigematsu, "Axial microscopic distribution of grown-in defects in Czochralski-grown silicon crystals," *Jpn. J. Appl. Phys., Part 2* **32**, L699 (1993).
- <sup>3</sup>M. Kato, T. Yoshida, Y. Ikeda, and Y. Kitagawa, "Transmission electron microscopy observation of IR scattering defects in as-grown Czochralski Si crystals," *Jpn. J. Appl. Phys., Part 1* **35**, 5597–5601 (1996).
- <sup>4</sup>S. S. Pascoa, "Oxygen and related defects in Czochralski silicon crowns," M.S. thesis, Norwegian University of Science and Technology, 2014.
- <sup>5</sup>Y. Yoshida and G. Langouche, *Defects and Impurities in Silicon Materials* (Springer, 2015).
- <sup>6</sup>S. Umeno, M. Okui, M. Hourai, M. Sano, and H. Tsuya, "Relationship between grown-in defects in Czochralski silicon crystal," *Jpn. J. Appl. Phys., Part 2* **36**, L591–L594 (1997).

- <sup>7</sup>V. Monier, L. Capello, O. Kononchuk, and B. Pichaud, "Light scattering from dislocations in silicon," *J. Appl. Phys.* **108**, 093525 (2010).
- <sup>8</sup>K. Moriya and T. Ogawa, "Observation of growth defects in synthetic quartz crystals by light-scattering tomography," *J. Cryst. Growth* **44**, 53–60 (1978).
- <sup>9</sup>K. Moriya and T. Ogawa, "Observation of lattice defects in GaAs and heat-treated Si crystals by infrared light scattering tomography," *Jpn. J. Appl. Phys., Part 2* **22**, L207–L209 (1983).
- <sup>10</sup>R. Takade, N. Inoue, K. Moriya, K. Kashima, K. Nakashima, M. Kato, S. Kitagawa, T. Ono, H. Urushido, N. Nango, and V. Akhmetov, "Standardization of test methods for bulk micro-defects and denuded zones in annealed CZ Si," *ECS Trans.* **2**, 471–484 (2006).
- <sup>11</sup>K. Sakai, "Detection limit for defect density by light scattering tomography," *Jpn. J. Appl. Phys., Part 1* **45**, 7181–7183 (2006).
- <sup>12</sup>N. Nango, T. Ogawa, and T. Irisawa, "Minimum size of oxygen precipitates in Czochralski silicon wafers detected by improved light scattering tomography," *Jpn. J. Appl. Phys., Part 1* **44**, 5898–5902 (2005).
- <sup>13</sup>F. Korsós, L. Roszol, F. Jay, J. Veirman, A. D. Draoua, M. Albaric, T. Szarvas, Z. Kiss, A. Szabó, I. Soczó, G. Nádudvari, and N. Laurent, "Efficiency limiting crystal defects in monocrystalline silicon and their characterization in production," *Sol. Energy Mater. Sol. Cells* **186**, 217–226 (2018).
- <sup>14</sup>R. Duru, D. Le-Cunff, M. Cannac, N. Laurent, L. Dudas, Z. Kiss, D. Cseh, I. Lajtos, F. Jay, and G. Nadudvari, "Photoluminescence for in-line buried defects detection in silicon devices," in *2017 28th Annual SEMI Advanced Semiconductor Manufacturing Conference (ASMC)* (IEEE, 2017), pp. 262–266.